Microwave-green synthesis of AlPO-n and SAPO-n (n = 5 and 18) nanosized crystals and their assembly in layers

Eng-Poh Ng, Hussein Awala, Sarah Komaty, Svetlana Mintova

Microwave-green synthesis of AlPO-*n* and SAPO-*n* (*n* = 5 and 18) nanosized crystals and their assembly in layers

Eng-Poh Ng,[1] Hussein Awala,[2] Sarah Komaty,[2] Khaled Karaka,[2] Svetlana Mintova[2,*]

[1]*School of Chemical Sciences, Universiti Sains Malaysia, 11800 USM, Penang, Malaysia*

[2]*Laboratoire Catalyse et Spectrochimie (LCS), Normandie University, ENSICAEN, UNICAEN, CNRS, 14000 Caen, France*
**Corresponding author: mintova@ensicaen.fr*

ABSTRACT

Green synthesis of nanosized AlPO-*n* and SAPO-*n* (*n* = 5 and 18) crystals with AFI and AEI type structures from non-reacted precursor suspensions with an essential chemical compensation is presented. The crystallization of both materials was accomplished within few minutes (5-18 minutes) instead of several days by replacing the conventional with microwave heating. The nanosized AlPO-*n* and SAPO-*n* (*n* = 5 and 18) crystals were stabilized in coating suspensions and deposited in layers on silicon wafers. It is shown that the AFI-type crystals (one-dimensional pores with a diameter of 0.73 nm) were primarily oriented with (001) direction perpendicular to the substrate, while the AEI-type crystals (three-dimensional pores with a diameter of 0.38 nm) were randomly oriented. The relationship between the crystal orientation and the adsorption behavior of the AFI and AEI layers toward water was studied by GI-XRD and operando IR spectroscopy.

Keywords: AlPO-*n*, SAPO-*n*, nanocrystals, microwave synthesis, layers, orientation, water adsorption.

1. INTRODUCTION

Zeolites and related crystalline solids (zeotypes) are microporous materials with defined pores less than 1.2 nm in diameter [1]. They have been widely used in catalysis, ion exchange and separation processes [2, 3]. A special attention has been focused on the synthesis of nanosized microporous materials (less than 400 nm) [3–5], *i.e.*, that can be easily

assembled in thin-to-thick layers and readily used for new applications including chemical sensors [6,7], microelectronic devices [8], microreactor [9,10], medicine [11], low-*k* dielectric films [12,13] and selective membrane [14,15].

The zeolite nanocrystals are commonly synthesized from clear precursor suspensions with a large consumption of organic templates under conventional heating [16, 17]. After the synthesis is completed, the nanocrystals are separated while the non-reacted solution is discarded, resulting in the disposal of expensive chemical reagents with detrimental environmental effects. In respect to this, the reuse of the non-reacted chemicals for multi-step synthesis of both micron-sized (BEA, FAU) [18, 19] and nanosized (LTA, FAU, MFI, CHA) [20–23] zeolites for increase the crystalline yield has been reported. The main concept of this approach is to reuse the non-reacted mixtures after recovering the solid products from the solution, followed by chemical compensation (if needed) for subsequent cycles of synthesis. Thus, this approach enables a substantial rise in the crystalline yield of the materials and keeps the particle size constant, while making the synthesis more efficient.

In addition to zeolites, nanosized aluminophosphates (AlPO-*n*) and isomorphous substituted aluminophosphates with various metals (SAPO-*n*, MeAPO-*n*) have been synthesized by hydrothermal [24, 25], ionothermal [26], microwave assisted hydrothermal [27] and ultrasonic wave-assisted hydrothermal [28] approaches. The syntheses of AlPO-*n* and SAPO-*n* are commonly performed at temperature higher than 160 °C, and the inclusion of an organic structure-directing agent, usually an amine, is essential in producing the microporous framework. Among the zeotype materials, only AlPO-5 [27, 29], MnAlPO-5 [26], AlPO-18 [24] and SAPO-34 [30] and AlPO-41 [25], have been successfully synthesized with nanosized dimensions.

The synthesis of nanosized AlPO-18 by using recycled and non-reacted chemical reagents has been reported [20]. The mother liquor was used up to several cycles while the crystalline yield was increased, and the morphology and particle size distribution were preserved. However, the feasibility of using this recycled chemical solution for the synthesis of various types of nanosized zeotype materials is considerably new, and it is the basis of this study.

In this paper the microwave-green synthesis of AEI-type (AlPO-18, SAPO-18) and AFI-type (AlPO-5, SAPO-5) molecular sieves by using non-reacted precursor suspensions

(mother liquor) followed by essential chemical compensation is presented. Unlike conventional hydrothermal treatment, microwave (MW) irradiation is used since it provides a new, fast, efficient and environmentally benign methodology for the synthesis of nanosized molecular sieves. The MW causes homogeneous heating, high reaction rate, high selectivity and increased product yield [31]. The AEI- and AFI-type materials are synthesized with nanosized crystals less than 300 nm and further assembled in layers by spin coating approach.

2. EXPERIMENTAL SECTION

2.1. Microwave-green syntheses of AlPO-n and SAPO-n nanosized crystals

The AlPO-18 was obtained under hydrothermal treatment of a mixture containing aluminum isopropoxide ($Al(OiPr)_3$), phosphoric acid (H_3PO_4), tetraethylammonium hydroxide (TEAOH) and water as reported elsewhere [20]. Typically, $Al(OiPr)_3$ (15.52 g) was completely dissolved in a mixture containing TEAOH solution (101.04 g, 35%, Aldrich) and water (57.38 g). Then H_3PO_4 (27.68 g, 85%, Aldrich) was slowly added in a drop-wise manner with continuous stirring. The resulting transparent solution was divided into 8 × 25 g portions and transferred in eight Teflon-lined ceramic autoclaves (50 ml). A microwave treatment of the suspensions using an Anton Paar Synthos 3000 oven was carried out with a temperature-programmed mode (2.5 min to reach 180 °C (power of 800 W), maintained for 5 min before cooling down to room temperature). The AlPO-18 crystalline products (yield 59.7 %) were separated by centrifugation (20000 rpm, 30 min), and the suspension containing non-reacted materials was preserved for the following syntheses with compensation of required amount of inorganic (Al, P), organic (TEAOH) sources and water.

Prior to the synthesis of AlPO-*n* and SAPO-*n* nanocrystals, the water (~35 %) from the non-reacted mixture was partially evaporated at 60 °C for 4 days until a viscous suspension was obtained. The chemical composition of the viscous suspension was then determined before the chemical compensation. The concentration of Al, P and N elements in the non-reacted suspension was 11376, 42203 and 197451 ppm, respectively, according to the ICP-OES analysis.

The chemical composition of non-reacted suspensions before and after chemical compensation used for the preparation of AlPO-*n* and SAPO-*n* (*n* = 5 and 18) are summarized in Table 1. During the compensation, appropriate amount of $Al(OiPr)_3$ was firstly mixed with

the required amount of TEAOH, and finally water was added until a clear or an homogenous white suspension were obtained. In some cases (e.g. AlPO-5 and SAPO-5), mechanical stirring was required since the resulting mixture gradually becomes viscous during the addition of H_3PO_4. For SAPO-5 and SAPO-18 systems, silica sol HS-30 (Sigma-Aldrich) was added in the end of the mixing process. The precursor suspensions were subjected to microwave heating and the conditions of the experiments are summarized in Table 1.

The solid products after the synthesis were separated from the suspensions using high-speed centrifugation (20000 rpm, 30 min). The crystalline materials were purified by series of centrifugation and ultrasonic re-dispersion in distilled water or water/ethanol (80/20) to obtain a concentration of the solid product of 3.0 wt.%. A half from the crystalline products were freeze-dried and calcined at 550 °C for 10 h with a heating ramp rate of 1 °C/min prior characterizations.

2.2. Preparation of AlPO-n and SAPO-n layers

The AlPO-*n* and SAPO-*n* layers were prepared by spin coating approach: (i) 0.25 ml of aqueous colloidal suspensions with a concentration of 1 wt.% was mixed with 0.05 ml of Acrylate-*tert*-butylacrylamide, and (ii) deposited onto preliminarily cleaned Si-substrates by acetone under ultrasonication for 15 min. Acrylate-*tert*-butylacrylamide was used as an organic binder to increase the mechanical stability and thickness of the layers. The speed and duration of the spinning rotation were 2500 min^{-1} and 30 s, respectively. In order to obtain thicker films, the coating procedure was repeated 2-to-5 times. The layers were annealed at 550 °C for 3 h with temperature acceleration of 2°C/min in order to remove the organic binder and the template from the channels of the AlPO-*n* and SAPO-*n* crystals. Layers with a thickness in the range 190 - 320 nm were prepared and selected samples were subjected to characterization.

2.3. Characterization

The crystallinity and purity of the samples were characterized by a PANalytical X'Pert PRO diffractometer with Cu K_α radiation (λ=0.15418 nm, 40 mA, 45 kV, step size of 0.02° and a scan speed of 1°/min). The crystal size and morphological features of the samples were examined by a Philips XL-30 scanning electron microscope (SEM). The particle size and

colloidal stability of the nanocrystals in water/ethanol (80/20) suspension were measured using dynamic light scattering (DLS) and zeta potential (ξ), respectively, with a Malvern Zetasizer Nano Series. The porosity of the samples was analyzed by a Micromeritics ASAP 2010 after degassing overnight at 300 °C. The chemical composition of the solid materials was determined by X-ray fluorescence (XRF) analysis with a MagiX PHILIPS PW2540. The initial and re-used suspensions were characterized with inductively coupled plasma optical emission spectroscopy (Varian Vista MPXICP-OES) and 2400 Series II CHNS/O elemental analyzer.

The crystalline nature of the layers and degree of disordering were investigated by grazing incident X-ray diffraction (GI-XRD) performed at the European Synchrotron Radiation Facility (ESRF), Grenoble, beam line ID 01. The wavelength (λ = 0.156 nm) was selected by a double crystal monochromator, and the incident angle (α_i) of the X-ray beam was varied from 0.1 ^{o} to 0.3^o. A position-sensitive detector placed perpendicular to the sample was used to collect the scattered signal from the samples.

2.4. AlPO-n and SAPO-n layers: water adsorption followed by operando IR spectroscopy

The water adsorption in the AlPO-*n* and SAPO-*n* layers was followed by *operando* IR spectroscopy. The IR reactor cell consists of a modified diffuse IR cell (diffuse reflectance accessory, Pike) and an environmental chamber for study of supported layers under control gas flow and temperature. The IR reactor cell is equipped with a heating system working at temperatures up to 300 °C. Prior to each measurement, the layers were activated at 250 °C for 3 h under argon (flow rate of 20 cc/min) in order to remove the water readily adsorbed. All experiments were carried out at atmospheric pressure. The water vapor was introduced via a saturator using the corresponding Antoine's coefficients to calculate the water flow at the desired temperature. The water vapor with Ar as a carrier gas was introduced in the IR cell as follows: activation flow, Ar with a total flow of 20 cc/min; reaction flow, water vapor with a concentration of 500-7000 ppm diluted in Ar with a total flow of 20 cc/min. The IR spectra were collected in a continuous mode (32scan/spectrum) with a Tensor 27 spectrometer (Bruker) equipped with a DTGS detector. The amount of water adsorbed in the layers was obtained by plotting the integrated area of the bands in the range 1520-1760 cm^{-1} versus the delivered quantity of water vapour.

3. RESULTS AND DISCUSSION

3.1. Microwave-green synthesis of AlPO-n and SAPO-n materials

The synthesis of AlPO-*n* and SAPO-*n* (*n* = 5, 18) under microwave-assisted hydrothermal crystallization was carried out using the non-reacted suspensions from the synthesis of nanosized AlPO-18 after separation of the crystalline nanoparticles (see Experimental Section 2.1). Large excess of organic templates (TEAOH) was used to control the particle size and the structure of the materials, and therefore in the suspensions a great amount of non-reacted organics was present. Besides, non-reacted phosphorous and aluminum were also present. After adjusting the chemical composition of the non-reacted suspensions from the synthesis of the AlPO-18, the crystallization of four types of materials, e.g.AlPO-5, SAPO-5, AlPO-18 and SAPO-18 was carried out.

The XRD patterns of the crystalline products are shown in Fig. 1. The patterns exhibit typical Bragg peaks of AEI-and AFI-type structures [32]. The highly intense Bragg peaks are broad due to the presence of highly crystalline small particles [33]. Single crystalline phases were obtained in most cases due to the optimal conditions used for the preparation of AEI- and AFI- type molecular sieves (proper chemical composition, temperature and heating time). While the crystallization of AlPO-18 and SAPO-18 required only 5 minutes, the crystallization of AlPO-5 and SAPO-5 is completed within 18 minutes. On the other hand, the crystallization temperature of the AEI-type materials is higher (180 °C) compared to that of the AFI-type crystals (140 °C). Thus, it can be concluded that the AFI-type molecular sieves, obtained at lower temperature, have lower activation energy for microporous crystal growth than AEI-type crystals. Furthermore, it is of significant importance to keep the temperature and the synthesis time constant to ensure that pure crystalline phase is obtained.

The formation mechanism of AlPO-*n* and SAPO-*n* molecular sieves was studied using NMR spectroscopy [34], UV-Raman spectroscopy [35], etc. [36]. A direct evidence of the existence of the secondary building unit (SBU) species in the precursor suspensions acting as building blocks in the subsequent formation of 3D molecular sieve architectures was found. In our case, the non-reacted liquid phase of the AlPO-18 might contain double 6-rings (D6R) SBUs. Thus, we believe that these SBUs play the role of crystal seeds during the formation

of AlPO-*n* and SAPO-*n* in the secondary synthesis step (both AEI- and AFI-type microporous solids have D6R SBU) [37].

The AEI- and AFI-type materials are further characterized by SEM (Fig.2). Both AlPO-5 and SAPO-5 have elongated hexagonal morphology and tend to agglomerate in needle-shaped crystals with a width of 85 nm and length of 160–1200 nm. The agglomerated AFI nanoparticles were also observed by Du et al. [38] and Mintova et al. [29], which is apparently due to the long microwave treatment. Additionally, a slight difference in the size and morphology is observed once the Si is introduced in the precursor suspensions used for the preparation of AFI-type sample. The AlPO-18 and SAPO-18 materials have elongated plate-like crystals with length/width aspect ratio of about 2, and the average particle size of AlPO-18 and SAPO-18 is 250 nm and 195 nm, respectively (random measurements of 100 crystals with SEM were performed). It is worth to mention that the AlPO-18 crystals obtained in this study have a size almost identical to the AlPO-18 synthesized in our previous work [20].

The particle size distribution and the colloidal stability of the crystals in the purified suspensions (pH = 7.5) were also measured. As illustrated in Fig.3a, the DLS curves for AEI (AlPO-18, SAPO-18) and AFI (AlPO-5, SAPO-5) suspensions represent a monomodal particle size distribution. The peaks with an extent from 100 to 600 nm and from 180 to 1000 nm for AEI- and AFI-type materials, respectively, are measured. The DLS data reveal that the mean crystal sizes of AlPO-18 and SAPO-18 are 240 nm and 190 nm, correspondingly, which is consistent with the SEM observations. The stability of the crystals in water/ethanol (80/20) suspension at 25 °C was also measured. It is found that the AEI-type crystals with smaller particle sizes have higher zeta potential value $|40\text{-}50\ \text{mV}|$ which explain the higher stability (Fig.3b) [39].

The porosity of the samples is characterized *via* nitrogen sorption measurements. All samples exhibited a Type I isotherm with a high nitrogen uptake at low P/P_o, which is a typical signature for microporous materials (Fig.4) [40]. The nitrogen uptake keeps increasing at high P/P_o range and a H1-H3 hysteresis loop [41] is also measured, which indicates the presence of textural mesoporosity originated from the small crystallite size. Furthermore, the presence of mesopores (>10 nm) in the samples is evidenced which is explained with good inter-particle packing order. The crystal size, BET specific surface and total pore volume of crystalline

AlPO-5, SAPO-5, AlPO-18 and SAPO-18 materials are summarized in Table 2. All molecular sieves have high specific surface area and high pore volume. For instance, a BET surface area of 594 m^2/g and a pore volume of 0.73 cm^3/g are measured for AlPO-18 sample. In addition, the highest pore volume (0.89 cm^3/g) is obtained for the SAPO-18, which is related to the smallest crystal size and largest textural mesoporosity of the sample. While the SAPO-5 has a pore volume of 0.52 cm^3/g and specific surface area of 548 m^2/g, which is due to partial aggregation of the crystals after drying prior the measurements. As expected, AlPO-5 and AlPO-18 have Al/P ratio equal to 1, while SAPO-5 and SAPO-18 have Si/(Al+P+Si) ratio of 0.07 and 0.001, respectively. Similar trend of low Si/(Al+P+Si) ratio was also observed for SAPO-34 nanocrystals [30]. Furthermore, high crystalline yield for all samples using the non-reacted synthesis solutions was achieved (see Table 2). The yield of AlPO-18 and AlPO-5 nanocrystalsis above 50 wt.% was measured, while a decrease of the yield to 45 wt.% under introduction of Si in both phases was achieved.

3.2. Deposition of AlPO-n and SAPO-n (n = 5, 18) nanocrystals in layers

The AFI- and AEI-type crystals were deposited on silicon wafers using spin-coating method. The SEM images of the AlPO-*n* and SAPO-*n* layers are presented in Fig. 5. The thickness of the layers is approximately 190–320 nm. No significant difference between the AlPO-5 and SAPO-5 layers is observed (Figs. 5a,b), and similar observation is made for the AlPO-18 and SAPO-18 layers (Figs. 5c,d).

The orientation and crystallinity of the nanocrystals in the layers were further investigated by GI-XRD. The GI-XRD patterns were recorded at different penetration depths by varying the angle of incidence (α_i = 0.3°, 0.2° and 0.1°). The GI-XRD patterns of AlPO-5 layers measured at α_i = 0.1° do not contain all Bragg peaks expected for the AFI-type material (Fig. 6A). For instance, the reflection with (hkl) value of (002) is not detected at low incident angle (α_i = 0.1°), which indicates that the c-axis of AFI molecular sieves is parallel to the substrate. At higher penetration depth measurements (α_i = 0.3°), the most intense Bragg peaks are appeared; however their intensity differs from that of the peaks in the powder sample (see Fig. 1a). For example, the intensity of the (211) peak is lower than (002), which is exactly the opposite for powder AFI-type sample (Fig. 1a). This observation can be explained with a partial orientation of the AlPO-5 elongated particles perpendicular to the support (Fig. 6a).

More pronounced difference is observed in the SAPO-5 layers, the (002) peak almost completely disappeared, and the (210) peak has higher intensity (Fig. 6b). This result indicates that the crystals are randomly oriented. It is important to note that the AFI-type crystals have one dimensional channel system with a pore opening of 0.73 nm, which are running along (001) direction. Thus for adsorption application, the orientation of the AFI-crystals will be of interest *via* proving access to the entire porosity of the layers.

For AlPO-18 layers, the Bragg reflections (002), (113/-113), and (114/-114), (132/-132) are not present in the XRD patterns collected at the three penetration depths (Fig. 6c). This observation is due to the fact that most of the crystals in the layers are oriented with the c-face perpendicular to the substrate. As the penetration depth was increased, an increased intensity of the peaks in the film was observed due to the improved density and better packing of the crystalline AlPO-18 particles; however the peaks mentioned above do not appear in the patterns. The GI-XRD data for the SAPO-18 layers have a different appearance, i.e. most of the Bragg peaks characteristics for powder samples appeared but with various intensity (Fig. 6d and Fig.1d). The incorporation of silicon in the AEI- and AFI-type framework structures alters but not significantly the size of the crystals and therefore a slightly different orientation of the particles deposited in the layers is observed.

3.2. Water adsorption on AlPO-n and SAPO-n (n = 5, 18) layers: operando IR study

A series of overlaid *operando* IR spectra (1400–1800 cm^{-1}) of the samples after water adsorption are presented in Fig. 7. The signals at the region of 1520-1760 cm^{-1}, which are assigning to deformation (or bending) vibrations of water molecules, increase as a function of water content adsorbed in the layers [42]. The corresponding plots deduced from the water adsorbed using the integrated IR areas (1520–1760 cm^{-1}) are shown in Fig. 8. As can be seen, AEI-type layer exhibits steeper slope than AFI-type counterparts indicating that the formal samples adsorb moisture faster than the latter at low water vapor pressure. Among the layers measured, AlPO-18 which has the highest surface area adsorbs the largest amount of water followed by SAPO-5, SAPO-18, AlPO-5.

Furthermore, it can be seen that the IR spectra recorded from the AEI and AFI layers differ markedly. For AlPO-5 and SAPO-5, a band at 1621–1625 cm^{-1} due to deformation vibration of H_2O molecule is detected after 500 ppm water was adsorbed. This band shifts to

1624–1631 cm^{-1} with increasing the water adsorbed. In addition, a weak shoulder is recorded for the AlPO-5 layer at 1710 cm^{-1} and SAPO-5 layer at 1699 cm^{-1}, upon adsorption of 500 ppm of water. This band is due to new bound or deformed H_2O (hydroxonium type) interacting *via* a bridging hydroxyl group with O atom of the neighboring H_2O molecule [43]. The position of this signal slightly shifts to higher wavenumber and the background becomes more intense with increase of water amount adsorbed. For AlPO-18 and SAPO-18, the O–H deformation vibration of H_2O appears at 1624–1629 cm^{-1} whereas the deformed H_2O resonates at 1686–1696 cm^{-1}. The intensity of both signals is increasing while the position of the bands is slightly blue-shifting upon further increasing the water amount adsorbed.

It is important to note that the crystal orientation of the AFI-type crystals is of significant importance since they have one-dimensional channel system, and their access is guaranteed if the crystals are oriented with (001) direction perpendicular to the support. While in the case of AEI-type crystals any orientation is sufficient due to its three-dimensional pore structure, and hence it will easily provide contact to their internal pore system. Moreover, the access in the pores will be enhanced if the crystals have nanosized dimensions. As a result, fast adsorption and high water adsorption capacity for the AEI-type layers were measured.

4. CONCLUSIONS

In summary, AlPO-*n* and SAPO-*n* (*n* = 5 and 18) nanocrystals are prepared using non-reacted precursor suspensions obtained from the synthesis of AlPO-18 crystals after slight adjustment of the chemical compositions. The use of microwave synthesis approach leads to the formation of either AlPO-*n* or SAPO-*n* nanocrystals within short time, thus having impact on energy saving issue. Moreover, a substantial minimizing in the amount of the hazardous chemicals (organic templates and phosphoric acid) as initial and waste is realized, and a high yield synthesis procedure for four types of microporous materials was established. The size of the crystals was in the nanometer range (< 300 nm) and furthermore, the AlPO-*n* and SAPO-*n* (*n* = 5 and 18) crystals stabilized in water/ethanol (80/20) suspension were used for preparation of layers on silicon wafers.

The high crystallinity of both layers and the slightly low orientation of the AFI-type crystals suggest low accessibility of water to the entire pore volume that is of main concerns for future applications such as in moisture and hydrocarbon sensing. On the other hand, the

AEI-type crystals with three-dimensional pores, which are randomly oriented on the silicon surface and small crystallite size will be very useful for selective and fast sorption applications.

Acknowledgement

The financial support from and Normandy C2-MTM Project is acknowledged.

References

[1] D.W. Breck, Zeolite Molecular Sieves; Wiley: USA, (1974).

[2] J.A. Martens, P.A. Jacobs, In Advanced Zeolite Science and Applications, Studies in Surface Science and Catalysis, J.C. Jansen, M. Stöcker, H.G. Karge, J. Weikamp, Eds.; Elsevier: The Netherlands, (1994) 85.

[3] V. Valtchev, L. Tosheva, Chem. Rev. 113 (2013) 6734-6760.

[4] L. Tosheva, V.P. Valtchev, Chem. Mater. 17 (2005) 2494-2513.

[5] J. Grand, H. Awala, S. Mintova, CrystEngComm 18 (2016) 650-664.

[6] L. Tosheva, E.-P.Ng, S. Mintova, M. Holzl, T.H. Metzger, A.M. Doyle, Chem. Mater. 20 (2008) 5721-5726.

[7] M.A. Urbiztondo, I. Pellejero, M. Villarroya, J. Sesé, M.P. Pina, I. Dufour, J. Santamaría, Sens. Actuators. B: Chem.137 (2009) 608-616.

[8] Y. G. Yan, T. Bein, Chem. Mater. 5 (1993) 905-907.

[9] E.E. McLeary, J.C. Jansen, F. Kapteijn, Micropor. Mesopor. Mater. 90 (2006) 198-220.

[10] Y. Zhang, Y. Liu, J. Kong, P. Yang, Y. Tang, B. Liu, Small 2 (2006) 1170-1173.

[11] C.P. Iglesias, L.V. Elst, W. Zhou, R.N. Muller, C.F.G.C Geraldes, T. Maschmeyer, J.A. Peters, Chem. Eur. J. 8 (2002) 5121-5131.

[12] Z.B. Wang, A.P. Mitra, H.T. Wang, L.M. Huang, Y. Yan, Adv. Mater. 13 (2001) 1463-1466.

[13] Z.B. Wang, H.T. Wang, A. Mitra, L.M. Huang, Y. Yan, Adv. Mater. 13 (2001) 746-749.

[14] L. Li, W. Yang, J. Membr. Sci. 316 (2008) 3-17.

[15] J. Caro, M. Noack, Micropor. Mesopor. Mater. 115 (2008) 215-233.

[16] S. Mintova, N. H. Olson, V. Valtchev, T. Bein, Science 283 (1999) 958-960.

[17] E.-P. Ng, G.K. Lim, G.-L. Khoo, K.-H.Tan, B.S. Ooi, F. Adam, T.C. Ling, K.-L. Wong, Mater. Chem. Phys. 155 (2015) 30-35.
[18] M.J. Eapen, K.S.N. Reddy, V.P. Shiralkar, Zeolites 14 (1994) 295-302.
[19] D.E.W. Vaughan, K.G. Strohmaier, US 5637287 (1997).
[20] E.-P. Ng, L. Delmotte, S. Mintova, Green Chem. 10 (2008) 1043-1048.
[21] O. Larlus, S. Mintova, T. Bein, Micropor. Mesop.Mater. 96 (2006) 405-412.
[22] W. Song, V.H. Grassian, S.C. Larsen, Chem. Commun. (2005) 2951-2953.
[23] D. Xi, Q. Sun, X. Chen, N. Wang, J. Yu, Chem. Commun. 51 (2015) 11987-11989
[24] H. van Heyden, S. Mintova, T. Bein, J. Mater. Chem. 16 (2006) 514-518.
[25] G. Majano, K. Raltchev, A. Vincente, S. Mintova, Nanoscale 7 (2015) 5787-5793.
[26] E.-P. Ng, S.S. Sekhon, S. Mintova, Chem. Commun. (2009) 1661-1663.
[27] E.-P. Ng, D.T.L. Ng, H. Awala, K.-L. Wong, S. Mintova, Mater. Lett. 132 (2014) 126-129.
[28] S. Askari, R. Halladj, Ultrason. Sonochem. 19 (2012) 554-559.
[29] S. Mintova, S. Mo, T.Bein, Chem. Mater. 10 (1998) 4030-4036.
[30] H. van Heyden, S. Mintova, T. Bein, Chem. Mater. 20 (2008) 2956-2963.
[31] G.A. Tompsett, W.C. Conner, K.S. Yngvesson, ChemPhysChem 7 (2006) 296-319.
[32] Atlas of zeolite framework types; http://www.iza-structure.org
[33] E.-P. Ng, H. Awala, K.-H. Tan, F. Adam, R. Retoux, S. Mintova, Micropor. Mesopor. Mater. 204 (2015) 204-209.
[34] F. Taulelle, M. Haouas, C. Gerardin, C. Claude Estournes, T. Loiseau, G. Ferey, Colloid Surface A 158 (1999) 299-311.
[35] F. Fan, Z. Feng, K. Sun, Q. Guo, Y. Song, W. Li, C. Li, Angew. Chem. Int. Ed. 48 (2009) 8743-8747.
[36] A.M. Beale, M.G. O'Brien, M. Kasunic, A. Golobic, M.S. -Sanchez, A.J.W. Lobo, D.W. Lewis, D.S. Wragg, S. Nikitenko, W. Bras, B.M. Weckhuysen, J. Phys. Chem. C 115 (2011) 6331-6340.
[37] H. van Koningsveld, Schemes for Building Zeolite Framework Models, http://www.iza-structure.org/databases/
[38] H. Du, M. Fang, W. Xu, X. Meng, W. Pang, J. Mater. Chem. 7 (1997) 551-555.
[39] T. Maurer, B.K. -Czarnetzki, Helv. Chim. Acta 84 (2001) 2550-2556.

[40] K.S.W. Sing, D.H. Everett, R.A.W. Haul, L. Moscou, R.A. Pierotti, J. Rouquerol, T. Siemieniewska, Pure Appl. Chem. 57 (1985) 603-619.

[41] A.V. Neimark, Stud. Surf.Sci. Catal. 62 (1991) 67-74.

[42] E.-P. Ng, S. Mintova, Microchem. J. 98 (2), 177-185

[43] M.M. Dubinin, A.A. Isirikyan, D.I. Mirzan, IzvestiyaAkademiiNauk SSSR, 8 (1974) 1699-1705.

Graphical abstract

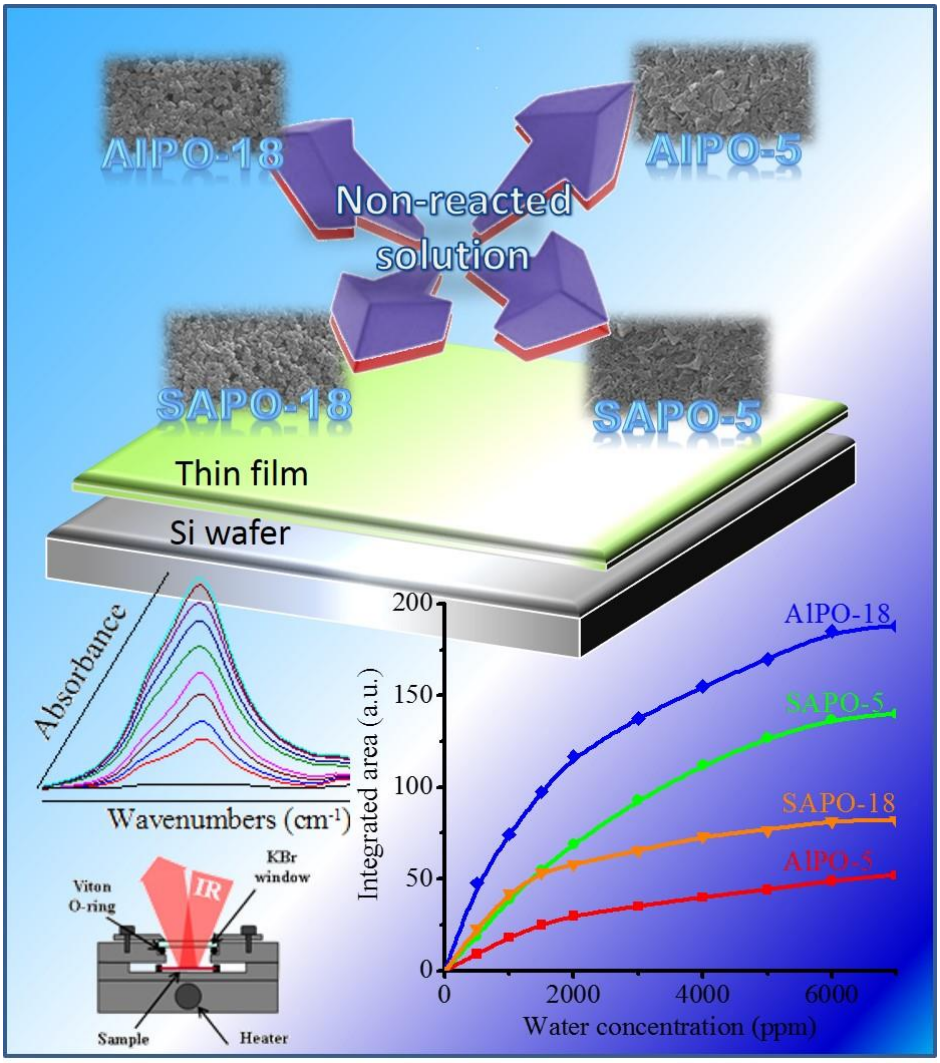

Highlights:

- Green synthesis of nanosized AlPO-*n* and SAPO-*n* (*n* = 5 and 18)
- Nanosized AlPO-*n* and SAPO-*n* crystals with high yield
- Orientation of AlPO-*n* and SAPO-*n* nanocrystals in layers
- Water sorption capacity of AlPO-*n* and SAPO-*n* layers

Tables

Table 1. Chemical compositions of precursor suspensions and synthesis conditions used for preparation of AlPO-*n* and SAPO-*n* (*n* = 5 and 18) materials using a microwave-green synthesis approach.

Samples	**Molar ratio**					**Synthesis condition**	
	Al_2O_3	**P_2O_5**	**TEA_2O**	**H_2O**	**SiO_2**	**T (°C)**	**t (min)**
Initial mother liquor	1.00	3.16	3.16	186	0.0	---	---
Non-reacted mother liquor	0.48	1.41	1.51	89[a]	0.0	---	---
AlPO-5	1.00	1.40	1.00	110	0.0	140	18
SAPO-5	1.00	2.10	1.50	100	0.6	140	18
AlPO-18	1.00	3.25	3.16	186	0.0	180	5
SAPO-18	1.00	2.05	2.00	100	0.6	180	5

[a]After partial water evaporation at 60 °C.

Table 2. Crystalline yield, size, zeta potential, chemical composition, pore volume and specific surface area of samples AlPO-5, SAPO-5, AlPO-18 and SAPO-18.

Samples	Yield[a] (wt.%)	Mean crystal size (nm)	Zeta potential (mV)	Total pore volume(cm^3/g)	Specific surface area(m^2/g)[b]	Al/P ratio
AlPO-18	52	250	-40	0.73	594	1.0
SAPO-18	44	195	-49	0.89	573	0.1[c]
AlPO-5	57	365	-33	0.61	548	1.0
SAPO-5	45	400	-26	0.52	597	7.0[c]

[a] $Crystallin\,e\ yield\ (\%) = \frac{Weight\ of\ solid\ product\ (g)}{Initial\ weight\ of\ Al_2O_3\ and\ P_2O_5\ (g)} \times 100\%$

[b] *Calculated by BET method*

[c] $Si/(Al + P + Si)\ ratio\ (\times 10^{-2}\ )$

Figure captions

Fig. 1 XRD patterns of samples (a) AlPO-5, (b) SAPO-5, (c) AlPO-18, and (d) SAPO-18 crystallized from chemically adjusted non-reacted suspensions using microwave-green synthesis approach.

Fig. 2 SEM images of (a) AlPO-5, (b) SAPO-5, (c) AlPO-18, and (d) SAPO-18 crystals synthesized from non-reacted suspensions after chemical adjustment.

Fig. 3 (a) Particle size distribution and (b) zeta potential values of AlPO-5, SAPO-5, AlPO-18, and SAPO-18 crystals in water suspensions (pH = 7.5, solid concentration of 3 wt.%).

Fig. 4 Nitrogen adsorption/desorption isotherms of (a) AlPO-5, (b) SAPO-5, (c) AlPO-18, and (d) SAPO-18 (solid and open symbols denote adsorption and desorption, respectively).

Fig. 5 SEM micrographs of (a) AlPO-5, (b) SAPO-5, (c) AlPO-18, and (d) SAPO-18 layers deposited on silicon wafers by spin coating approach. *Inset:* Cross-sectional view of the layers.

Fig. 6 GI-XRD patterns of spin coated (a) AlPO-5, (b) SAPO-5, (c) AlPO-18, and (d) SAPO-18 layers on silicon wafers at grazing incident angle (α_i): (a) 0.3°, (b) 0.2°, and (c) 0.1°.

Fig. 7 FTIR spectra collected from water adsorbed on (a) AlPO-5, (b) SAPO-5, (c) AlPO-18, and (d) SAPO-18 layers. From bottom to top, the water content is increased in the following sequence: 0, 500, 1000, 1500, 2000, 3000, 4000, 5000, 6000 and 7000 ppm.

Fig. 8 Adsorption capacity of samples toward water expressed as FTIR-integrated area (1400–1800 cm^{-1}) vs. concentration of water (500-7000 ppm) for (a) AlPO-5, (b) SAPO-5, (c) AlPO-18, and (d) SAPO-18 layers.

Figures

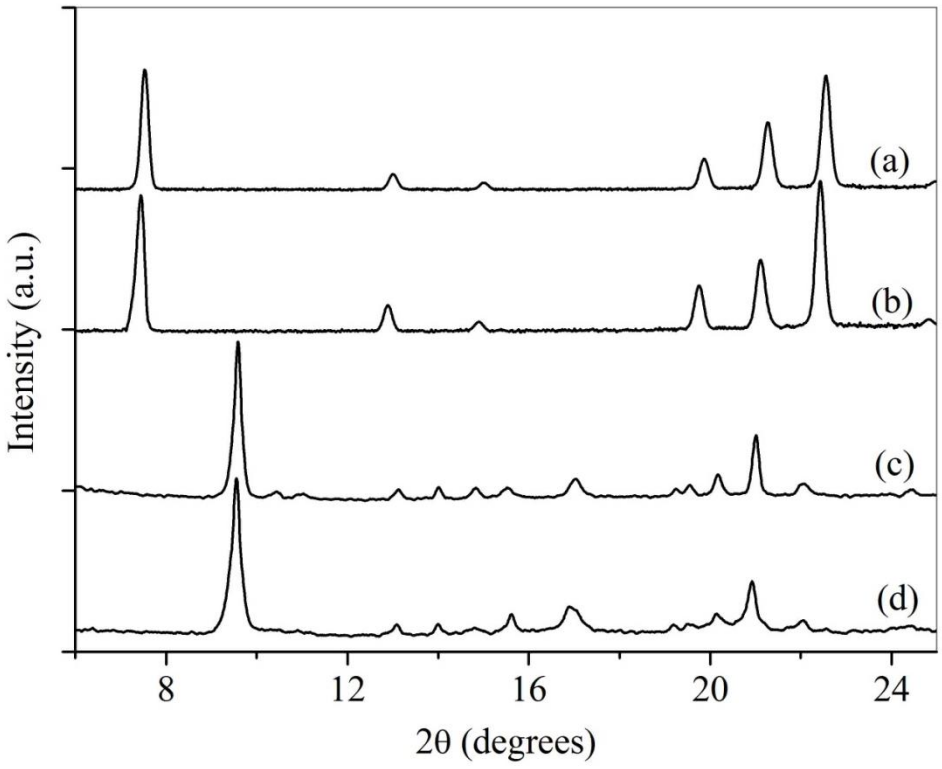

Fig. 1

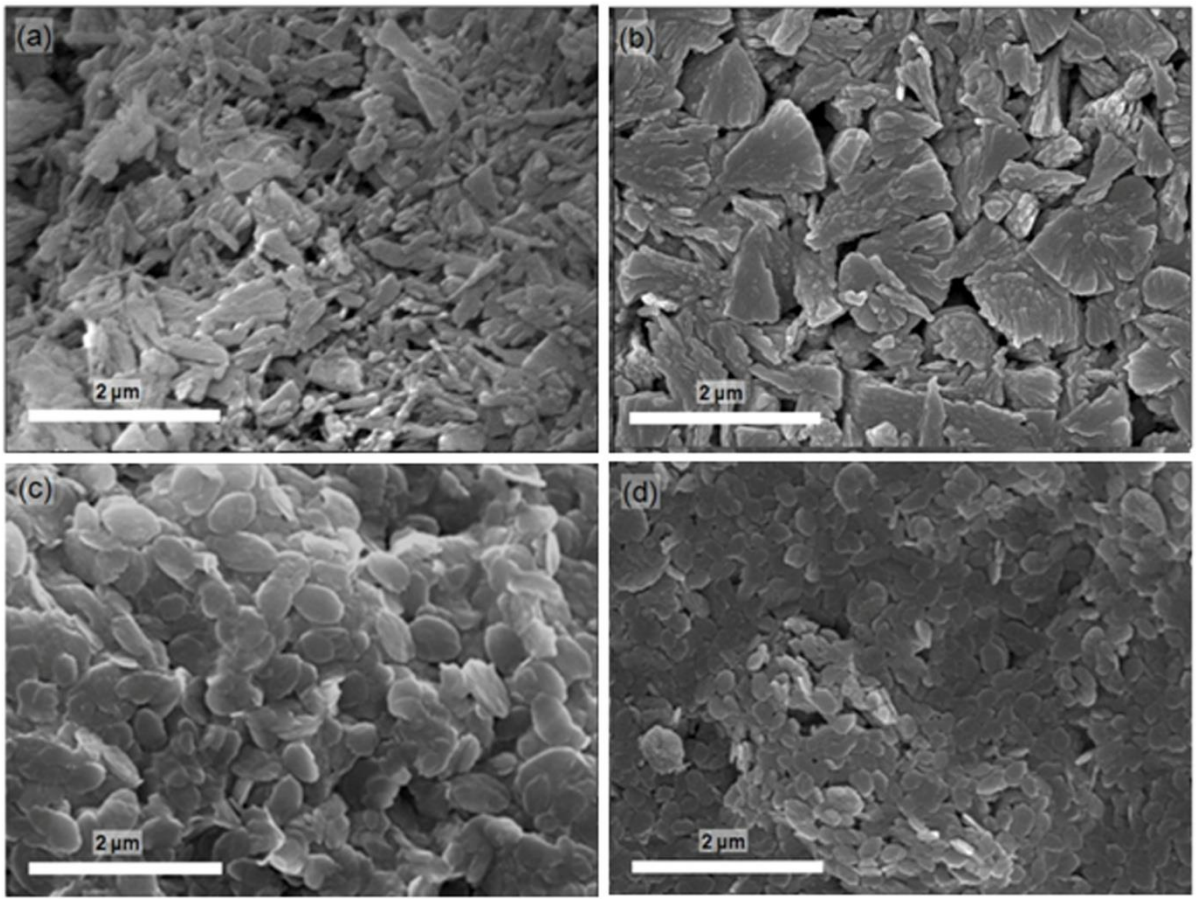

Fig. 2

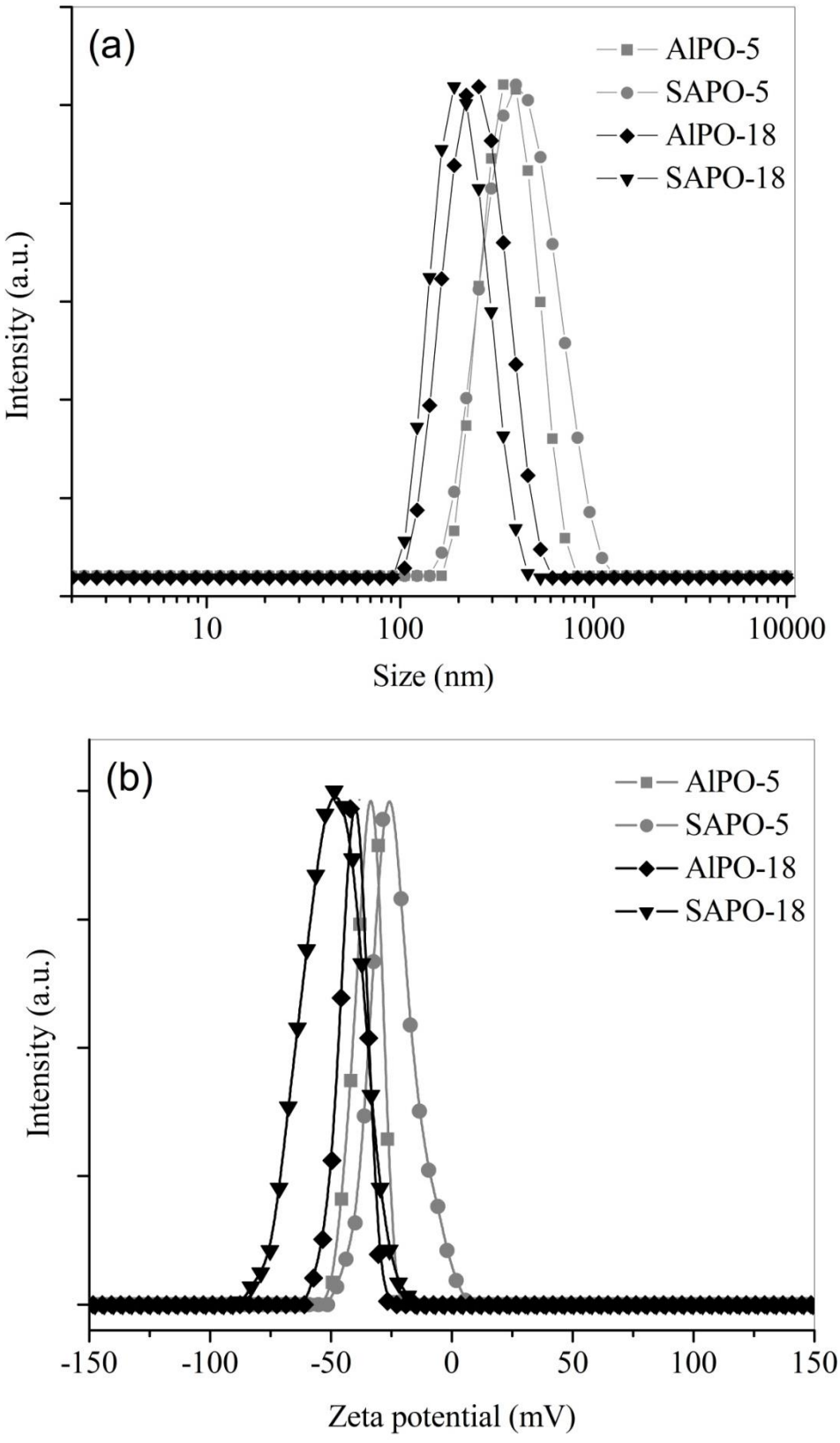
(a)
AlPO-5
SAPO-5
AlPO-18
SAPO-18
Intensity (a.u.)
10
100
1000
10000
Size (nm)
(b)
AlPO-5
SAPO-5
AlPO-18
SAPO-18
Intensity (a.u.)
-150
-100
-50
0
50
100
150
Zeta potential (mV)

Fig. 3

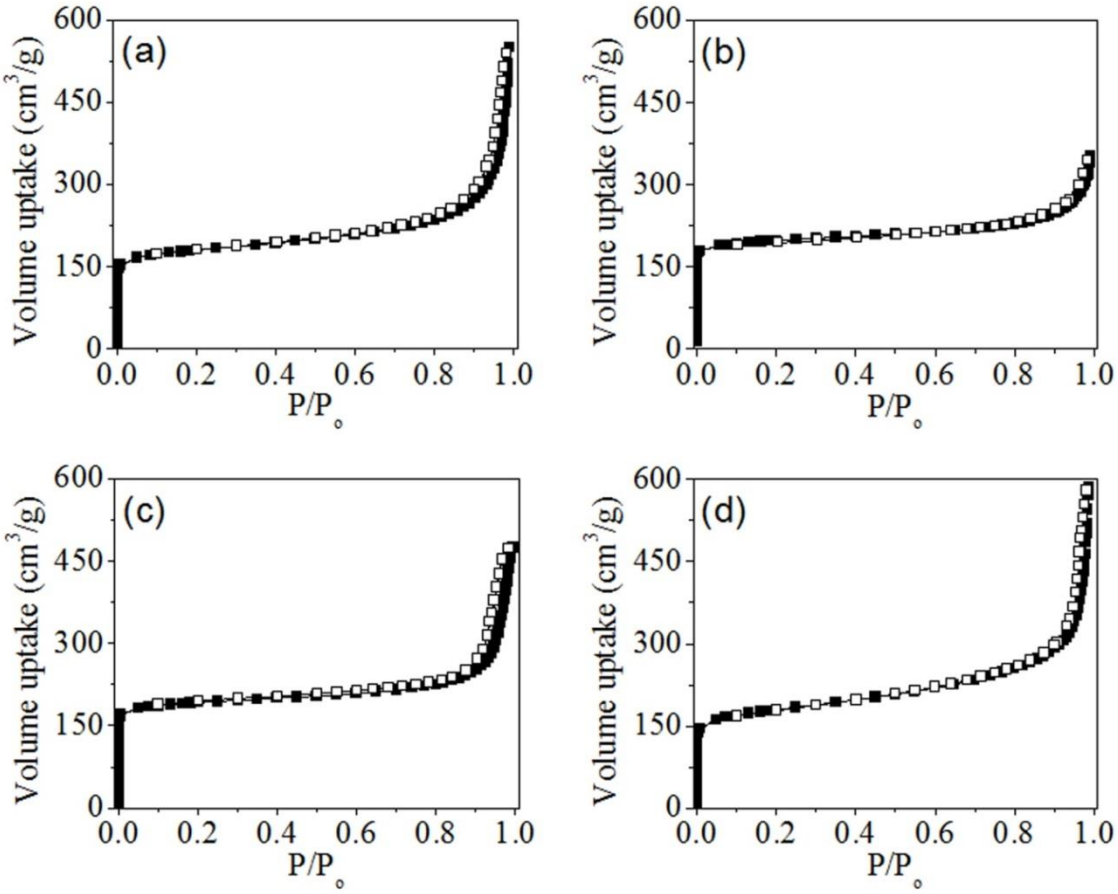

Fig. 4

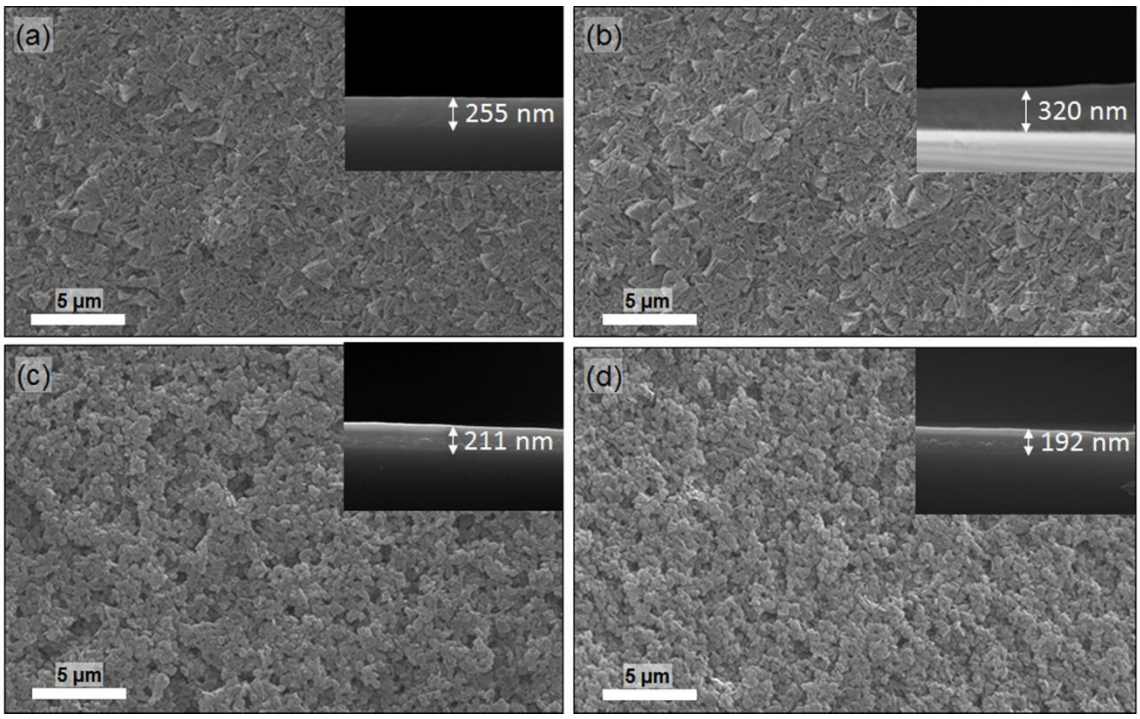

Fig. 5

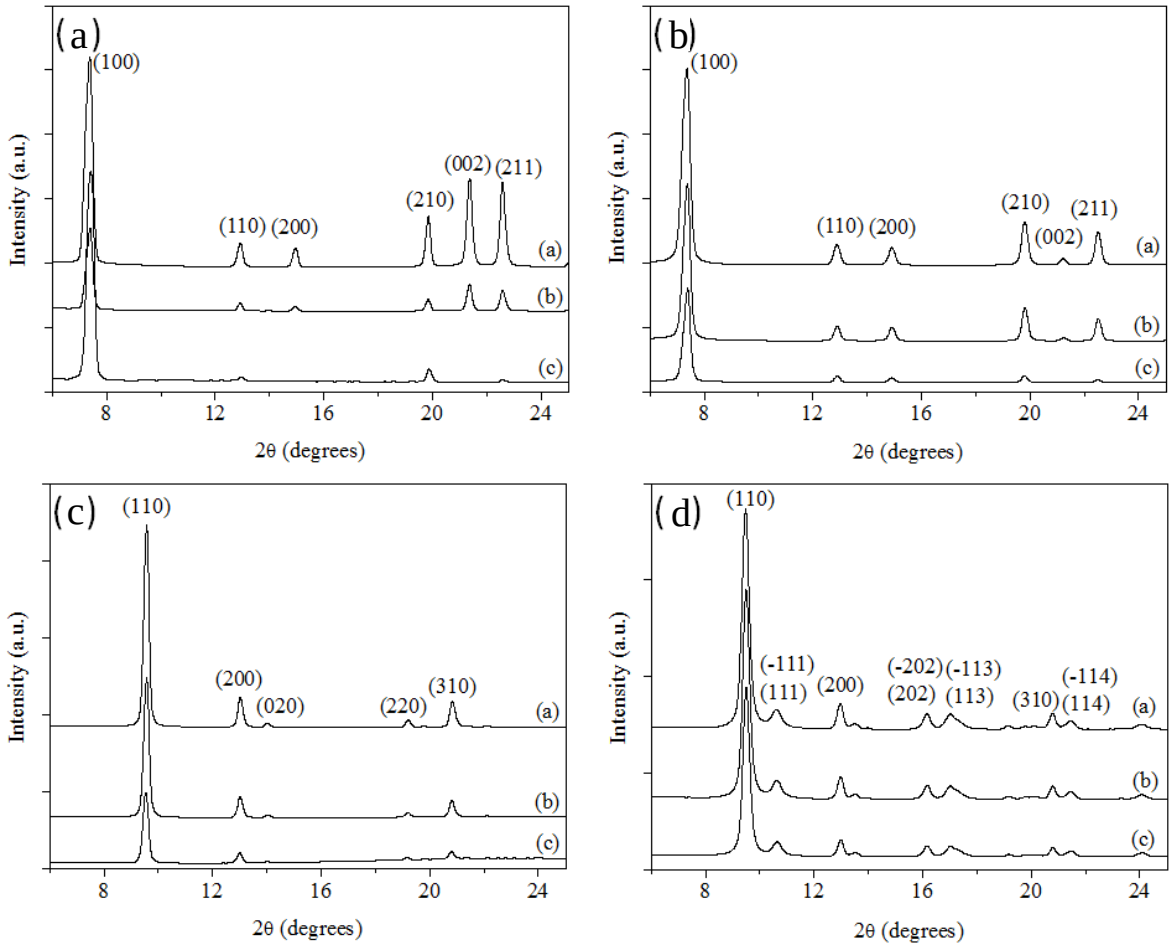
(a)
(100)
(110) (200)
(210)
(002) (211)
(a)
(b)
(c)
Intensity (a.u.)
2θ (degrees)
(b)
(100)
(110) (200)
(210)
(002)
(211)
(a)
(b)
(c)
Intensity (a.u.)
2θ (degrees)
(c)
(110)
(200)
(020)
(220)
(310)
(a)
(b)
(c)
Intensity (a.u.)
2θ (degrees)
(d)
(110)
(-111)
(111)
(200)
(-202)
(202)
(-113)
(113)
(310)
(-114)
(114)
(a)
(b)
(c)
Intensity (a.u.)
2θ (degrees)

Fig. 6

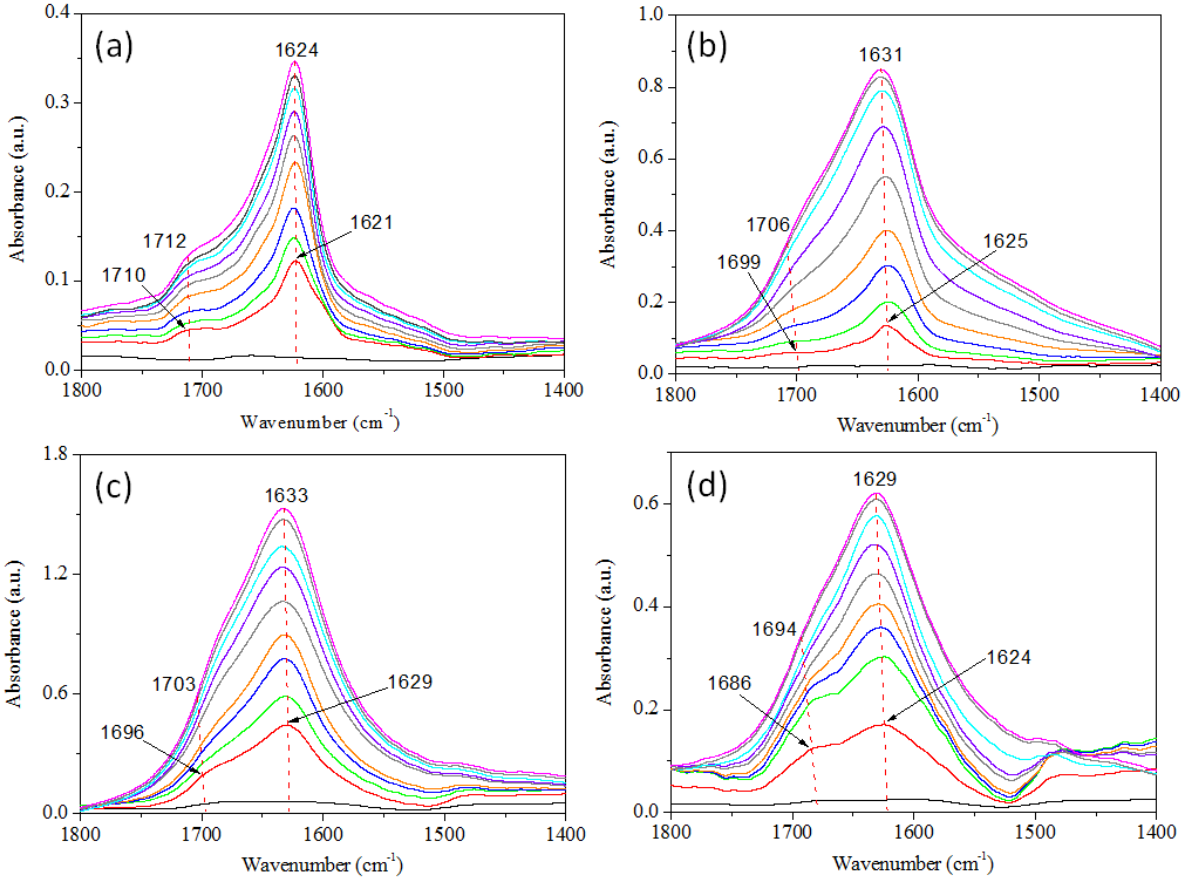
(a)
1624
1712
1710
1621
Absorbance (a.u.)
Wavenumber (cm-1)
(b)
1631
1706
1699
1625
Absorbance (a.u.)
Wavenumber (cm-1)
(c)
1633
1703
1696
1629
Absorbance (a.u.)
Wavenumber (cm-1)
(d)
1629
1694
1686
1624
Absorbance (a.u.)
Wavenumber (cm-1)

Fig. 7

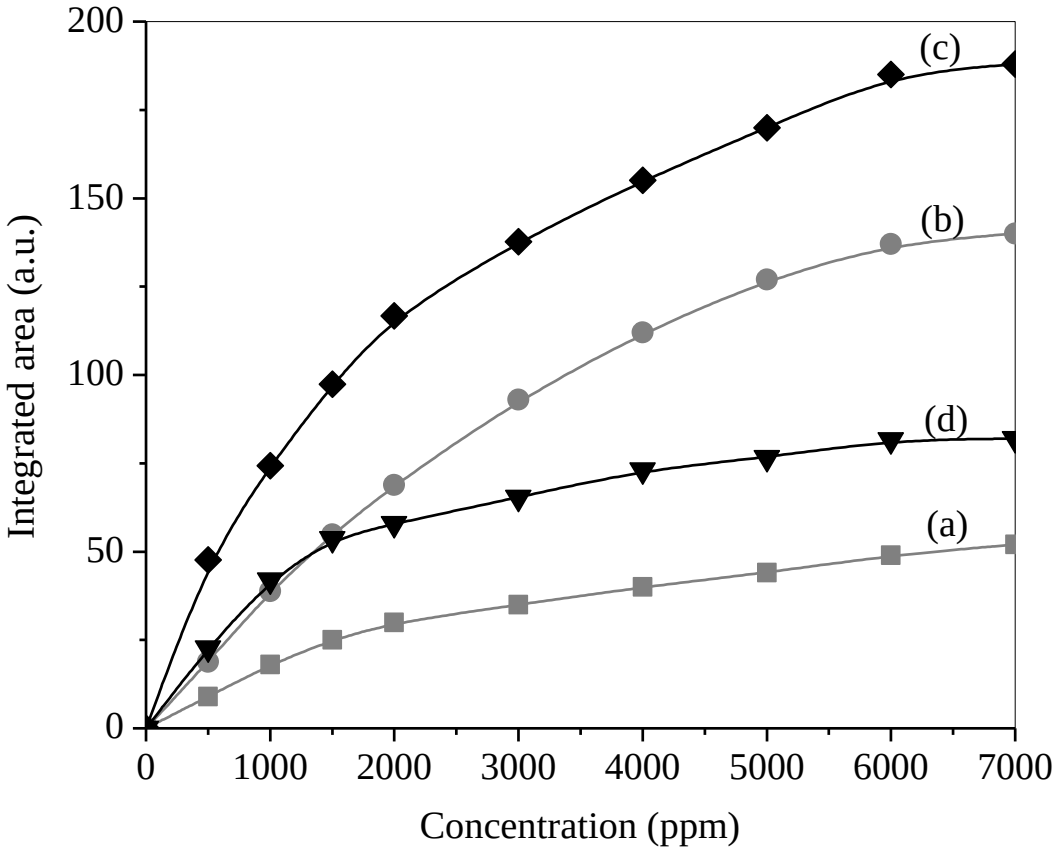
200
150
100
50
0
Integrated area (a.u.)
0
1000
2000
3000
4000
5000
6000
7000
Concentration (ppm)
(c)
(b)
(d)
(a)

Fig. 8.